DOI: 10.13009/EUCASS2023-384
Aerospace Europe Conference 2023 – 10TH EUCASS – 9TH CEAS

Multifidelity Aerodynamic Analyses of a Hybrid Laminar Flow Control and Variable Camber Coupled Wing

Mauricio M. Jentys ⋆†*, Tim Effing* ‡*, Christian Breitsamter* ⋆ *and Eike Stumpf* ‡
⋆*Chair of Aerodynamics and Fluid Mechanics, Technical University of Munich*
Boltzmannstr. 15, 85748, Garching bei München, Germany
‡*Institute of Aerospace Systems, RWTH Aachen University*
Wuellnerstr. 7, 52062, Aachen, Germany
mauricio.jentys@tum.de · effing@ilr.rwth-aachen.de
†Corresponding author

Abstract

This paper presents aerodynamic analyses of a transonic transport aircraft wing equipped with hybrid laminar flow control and variable camber systems. The analyses are performed on multiple fidelity levels, where particular focus within this paper lies on the efficient introduction of the high-fidelity (HiFi) computational fluid dynamics (CFD) results into the aerodynamic module of the overall aircraft design suite MICADO, representing the low-fidelity (LowFi) level. The introduction on integral coefficient level is achieved via the formulation of a Gaussian process regression-based surrogate model (SG) for the drag coefficient of the wing.Surface pressure distributions are predicted with a reduced-order model (ROM) utilizing Proper Orthogonal Decomposition. The predictions of both models are in good agreement with HiFi CFD results. Integrating the SG/ROM into the LowFi-environment reveals that both LowFi and HiFi approaches correspond well in predicting parametric sensitivities. Nevertheless, the SG/ROM integration substantially improves aerodynamic prediction accuracy at moderate computational and modeling costs.

1. Introduction

Current transonic transport aircraft designs possess a high level of maturity with respect to the key driving parameter of operational efficiency. To put this into context, within the time scope of 1960 to 2019, an average block fuel reduction of 1.3 % per year has been achieved for new aircraft entering the market. Nevertheless, comprehensive studies reveal further potential regarding this metric, namely an increase of up to 2.2 % compound reduction in block fuel intensity being possible through the year 2034 [1].

A decisive lever for efficiency gain acceleration is further increasing the aerodynamic performance of next generation aircraft. Especially modern technology bricks play a major role in this context, where two of the most promising candidates are hybrid laminar flow control (HLFC) and variable camber (VC) technologies. Apart from their individual benefits, synergistic effects are expected to further increase the respective potentials, see Fig. 1 (left panel) for a schematic overview. A comprehensive assessment of the above-mentioned potential is the dedicated goal of the research project CATeW (*Coupled Aerodynamic Technologies for Aircraft Wings*), which has been established between the Institute of Aerospace Systems (ILR) of RWTH Aachen University and the Chair of Aerodynamics and Fluid Mechanics (AER) of the Technical University of Munich. According to the bilateral structure of the project, the analyses of the technology coupling are conducted on two different fidelity levels (see Fig. 1, right panel). The low-fidelity (LowFi) assessments performed at ILR use the overall aircraft design (OAD) toolchain MICADO[1], which is a crucial enabler for mission analyses and evaluation or optimization tasks on system level. These analyses are complemented by high-fidelity (HiFi) computational fluid dynamics (CFD) simulations, performed at AER, which are necessary for a detailed aerodynamic assessment of the technology coupling and associated interaction effects.

While computational power continuously increases, still, the cost of running a HiFi CFD simulation is orders of magnitude higher than those for the corresponding aerodynamic assessments performed within MICADO. In order to balance computational expenses versus accuracy, the loop within the project is closed via a coupling of results from the HiFi side to the LowFi-environment via surrogate (SG) or reduced order models (ROM).

[1]Multidisciplinary Integrated Conceptual Aircraft Design and Optimization environment [2, 3]; MICADO is an internal specialization of UNICADO [4] providing conceptual design methods with increased fidelity.

DOI: 10.13009/EUCASS2023-384

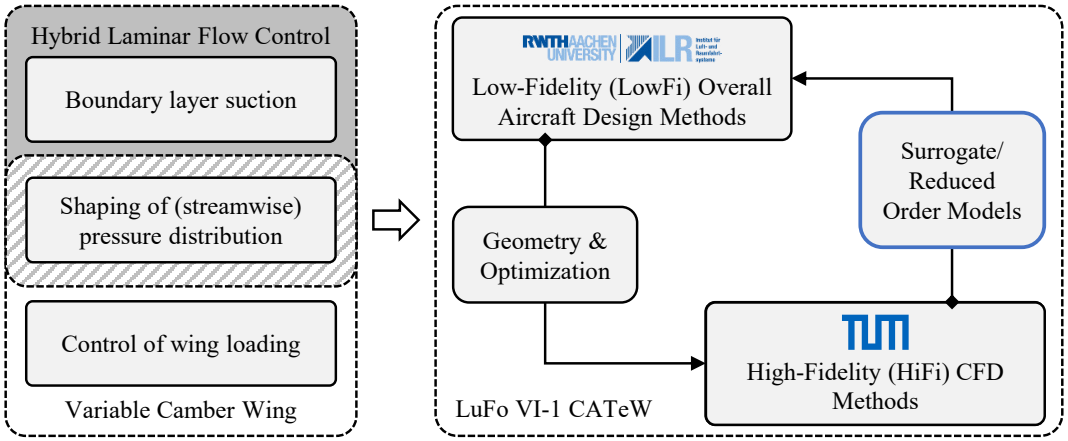

Figure 1: Overview of the envisaged technology coupling between HLFC and VC (left), with derived bilateral project framework and corresponding analysis fidelity levels (right).

Within this paper, coupling strategies between HiFi results and the aerodynamic toolchain of MICADO via different SG/ROM implementations are presented and assessed. According to the differentiation between SG and ROM, the models possess different degrees of abstraction. Performing parametric predictions of integral aerodynamic force coefficients is achieved through application of a Gaussian process regression (GPR) based SG, while prediction of aerodynamic surface quantities uses a ROM based on Proper Orthogonal Decomposition (POD). After a short introduction of the reference wing for the herein presented analyses (Sec. 2.1) and the LowFi (Sec. 2.3) and HiFi computational frameworks (Sec. 2.2), an overview of the implemented coupling strategies (Sec. 3), the theoretical background and conditioning aspects of the GPR-SG and the POD-ROM in the given context are presented in Secs. 3.1 and 3.2, respectively. Within Sec. 4.1, isolated model performance is assessed with respect to a test data set, after which results of the SG/ROM enhanced aerodynamic toolchain are discussed and compared to stand-alone LowFi results in Sec. 4.2. A summary and conclusions finalize the paper in Sec. 5.

2. Computational Frameworks

In the following, an overview of the geometry of the reference wing, alongside details regarding the HLFC suction panel and VC integration is presented. Section 2.2 elaborates on the applied CFD framework for simulation of the technology coupled wing, while the LowFi-environment, especially the corresponding aerodynamic module of MICADO is presented in Sec. 2.3.

2.1 Reference Geometry and Technology Integration

The planform view of the wing of the reference aircraft is depicted in the left panel of Fig. 2. The wing is extracted from the medium-range reference configuration CATeW-02 and consists of four sections S1-S4, according to the airfoils A1-A4. The geometry with a reference area of 220 m^2 has been derived at the ILR, based upon the AVACON research baseline 2028 [5]. Further details alongside geometrical and mission-specific parameters are summarized in Ref. [6]. For this contribution, out of the reference parameter set, the cruise lift coefficient of $C_L = 0.5$, the cruise Mach number of $\mathrm{Ma_{cr}} = 0.83$, and the initial cruise altitude of $H = 35\,000$ ft determine the SG and ROM prediction parameter spaces. Furthermore, VC integration to the wing is achieved via deflections of an Adaptive Dropped Hinge Flap (ADHF) [7, 8], as depicted in blue within the left panel of Fig. 2. The ADHF is primarily a high-lift device, nevertheless due to its kinematic foreseeing a Fowler motion of the main flap accompanied by a spoiler droop, multi-functionality in terms of a VC device is achieved for deflection angles between $\delta_{ADHF} = [-2°; 4°]$.
The second technology brick, namely the HLFC suction panel, is located on the upper side of the reference wing, depicted in red in the left panel of Fig. 2. Hybrid laminar flow control, according to the respective critical regions on swept aircraft wings, aims to suppress transition due to cross-flow instabilities (CFI) in the leading edge region of the wing through the application of boundary layer suction as a mean of active laminar flow control. Additionally, a suitable pressure distribution, namely a negative pressure gradient in chordwise direction within mid-chord stations of the wing, typically suffices to suppress the second dominant transition mechanism due to Tollmien-Schlichting instabilities (TSI) [9].

DOI: 10.13009/EUCASS2023-384

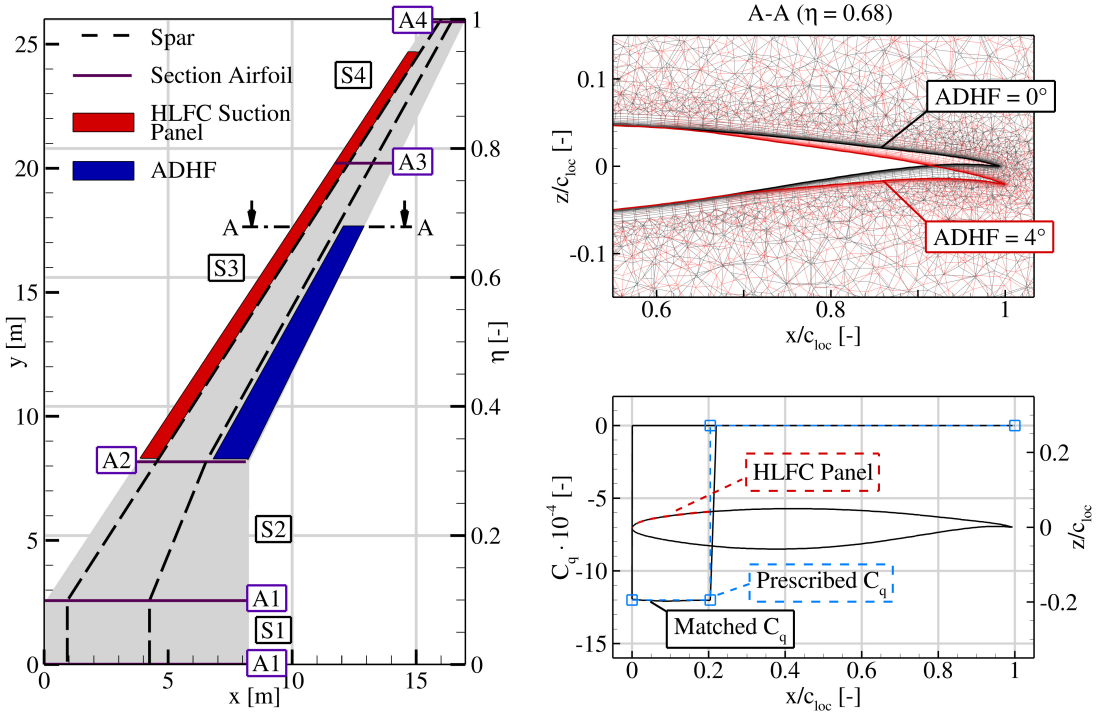

Figure 2: Left Panel: Planform view of the wing of the reference configuration CATeW-02 with indications of the extent of the HLFC suction panel and the ADHF. Right upper panel: Mesh deformation for a flap setting angle of $\delta_{ADHF} = 4°$ at $\eta = 0.68$. Right lower panel: Extracted suction coefficient distribution from CFD simulation at $\eta = 0.68$ (solid line), alongside prescribed distribution (dashed line).

2.2 High-Fidelity: Computational Fluid Dynamics Framework

As introduced in Sec. 1, the high-fidelity (HiFi) level of the analyses presented in this paper is formed by Reynolds-Averaged Navier-Stokes (RANS) computational fluid mechanics (CFD) simulations. The simulations are conducted within the environment of the DLR TAU code [10], expanded with an additional software framework for modeling the technology coupling.

An overview of two main modules of the software framework for modelling the HLFC and VC technologies is presented in the right panels of Fig. 2. Implications of different ADHF deflection angles are modeled by according mesh deformations using the radial basis function mesh deformation tool within TAU [11], see upper right panel of Fig. 2. Inclusion of boundary layer suction into the simulations is achieved by the second main module of the implemented software framework, which iteratively updates a per-node prescribed wall mass flux with the density distribution resulting from the simulations in order to match a user-prescribed suction coefficient C_q. The suction coefficient C_q thereby non-dimensionalizes the wall-normal velocity v_n with the free-stream velocity U_∞, as $C_q = v_n/U_\infty$. A comprehensive overview of both modelling techniques in the given context is presented in Ref. [6].

To assess the potential provided through the technology coupling, a further requirement on the CFD simulations is posed by the inclusion of transition prediction. Within the present contribution, the correlation-based $\gamma - \mathrm{Re}_\theta + CF$ [12] transition turbulence model is applied, using the $\gamma - \mathrm{Re}_\theta$ model for prediction of transition due to two-dimensional phenomena, such as TSI, and an extension based on the local helicity Reynolds number $\mathrm{Re}_{\mathrm{He}}$ for inclusion of CFI. Application of the $\gamma - \mathrm{Re}_\theta + CF$ requires a high resolution of the computational mesh, both for the prism layers and the surface mesh. Therefore, after performing a mesh independence study, a hybrid, unstructured mesh consisting of $52.9 \cdot 10^6$ ($34.8 \cdot 10^6$ prisms and $18.1 \cdot 10^6$ tetrahedra) has been applied for the CFD simulations.

The main focus of the CFD simulations within the given context lies on generation of the corresponding training data sets for the surrogate (SG) and reduced order models (ROM), which for the envisaged coupling strategies (see Sec. 3) consist in the parametric prediction of the wing drag coefficient C_D, computed through integration of pressure and friction drag components, and the distributions of the pressure coefficient c_p and skin friction vector components c_f in x-, y-, and z-directions. Therefore, a main requirement of the above introduced software framework lies on the automation of training data set generation for a user-prescribed set of input parameters $\boldsymbol{p}$, which is achieved by embedding of the software toolchain into a python framework developed at AER [6].

DOI: 10.13009/EUCASS2023-384

2.3 Low-Fidelity: Aerodynamic module in MICADO

In contrast to high-fidelity CFD simulations, the approach commonly used in overall aircraft design (OAD) involves determining drag components separately and then calculating the total drag by summing these components. In the aerodynamic module of MICADO, the basic approach combines the multi-lifting-line code LIFTING_LINE (LILI)[2] for induced drag and established semi-empirical relations for other components, such as viscous and wave drag. To improve the level of detail for applications involving HLFC, Risse [16] developed a 2.5D method, which replaces the semi-empirical relations from Raymer [17] and Korn-Mason [18, 19] previously used for wing viscous and wave drag. The 2.5D method is based on geometric and fluid mechanics transformation principles, enabling the iterative integration of the 2D Euler/Boundary layer flow solver MSES [20] with the 3D stability analysis program suite STABTOOL [21, 22]. The latter predicts the transition location based on N-factors of TSI and CFI using the e^N and the 2-factor N_{CF}-N_{TS} methods [23]. The critical N-factors are set to $N_{CF,crit} = 7.5$ and $N_{TS,crit} = 9$, as recommended by Ref. [24]. Furthermore, attachment line transition is evaluated using the Pfenninger-Poll criterion, derived from experimental tests conducted at ONERA wind tunnels [25].
Within the MICADO loop, the aerodynamic module calculates local lift distributions and induced drag for various predefined angles of attack using LILI. The wing drag is then determined by querying an aerodynamic database for different spanwise wing positions and their respective local lift coefficients. If a queried position lies between two specific geometric key points, interpolation is employed to obtain the corresponding data. Finally, the total wing drag is computed by summing the drag components associated with each section, weighted by their respective areas.
In recent years, modifications have been introduced to the aerodynamic module of MICADO based on insights from internal and external projects conducted at ILR. These modifications, proposed by Schültke [26], primarily involve the setup and processing of comprehensive data within the aerodynamic database. The new approach entails the creation of a database exclusively comprising aerodynamic 2D data, thereby decoupling MSES from STABTOOL. Consequently, the latter is now executed during the aerodynamic performance calculation. However, the fundamental concept of computing section polars for specified spanwise positions remains unchanged.
Although both approaches offer certain advantages, uncertainties arise from the (conical) transformation rules applied to geometry, freestream conditions, and pressure distributions. These uncertainties were already highlighted by Schültke [27] and Effing et al. [28]; evaluating their impact constitutes one of the objectives of the CATeW project.
The VC technology is implemented by setting up a database that holds aerodynamic data not only of clean airfoils associated with each geometric key point of the wing but also various permutations of eligible airfoils. The general idea is to compute drag polars for every conceivable permutation of airfoils along the wingspan and merge them based on a predefined criterion, such as the optimum lift-to-drag ratio. The generation of airfoil permutations is facilitated by an in-house tool, which creates ADHF airfoils based on predetermined geometric flap parameters while also considering the tracking of partially overlapping spoilers. For a comprehensive overview of the process chain employed to assess the simultaneous application of HLFC and VC in MICADO, the reader may refer to Ref. [29].

3. Coupling Strategies

As stated in Sec. 1, the coupling of HiFi data with the LowFi-toolchain generally aims at complementing the aerodynamic assessments of the integrated wing technologies. For this, different coupling strategies are possible, as illustrated in Fig. 3.[3] Note that without the HiFi model integration points highlighted in blue, Fig. 3 generally shows the process chain introduced in Sec. 2.3 for calculating an arbitrary point of the global wing polar.
A prerequisite for formulation of the coupling strategies is the definition of the corresponding model in- and outputs. The input parameters are the same in both cases, specifically geometrical permutations through different ADHF deflection angles, the suction strength (distribution) C_q introduced via the HLFC system, and a set of parameters primarily characterizing the freestream conditions, namely the desired wing lift coefficient C_L and the cruise Mach and Reynolds numbers. Since the present analyses focus on the cruise flight envelope of the aircraft, several constraints on the input parameter space can be formulated, an overview of which is presented in Tab. 1.
The desired model output depends on the coupling strategy, where the first coupling strategy intends to substitute the total wing drag coefficient with higher fidelity data. This strategy improves the final polar, which is of main interest when evaluating the synergistic potential of HLFC and VC. It is implemented through a surrogate model, whose structure and functionality are explained in Sec. 3.1.

[2]The LILI code has been developed at DLR [13, 14] and is often used in conceptual aircraft design because when compared to higher order methods such as RANS computations, it gives reasonable results even for transonic flow conditions [15].
[3]In CATeW, the scope is on multifidelity aerodynamic analyses, which is why no variable fidelity approaches are discussed.

DOI: 10.13009/EUCASS2023-384

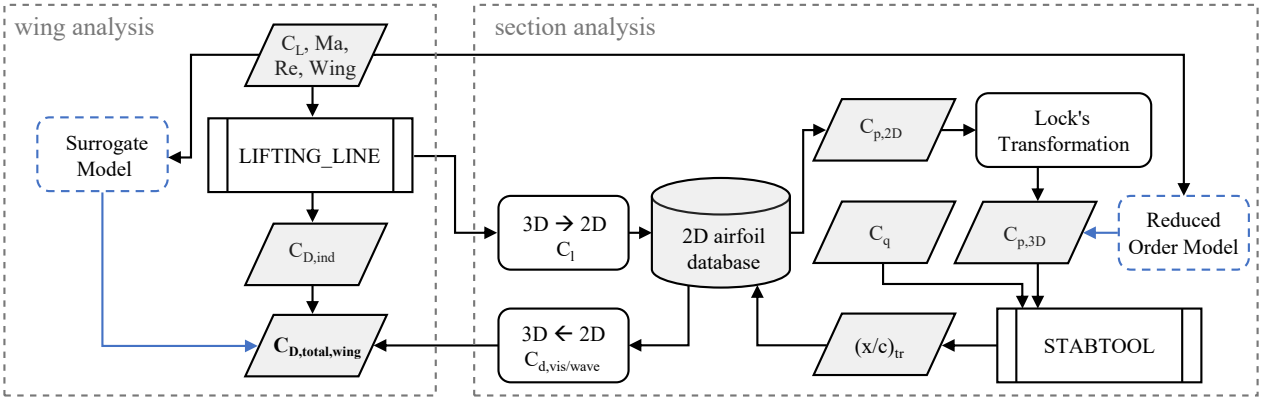

Figure 3: Overview of the calculation of an exemplary wing drag coefficient in MICADO with indication of SG and ROM integration points.

Table 1: Input parameter space for SG/ROM.

Parameter	Value	Comment
C_L	$[0.4; 0.6]$	Cruise $C_L = 0.5 \pm 0.1$
δ_{ADHF}	$[-2°; 4°]$	Flap-gap free deflection angles
H	[33 000 ft; 39 000 ft]	Resulting in Re $\approx [36.9; 28.8] \cdot 10^6$ at $\mathrm{Ma_{cr}}$
C_q	$-12 \cdot 10^{-4}$	Maximum extent of laminar flow predicted with $\gamma - \mathrm{Re}_\theta + CF$ model (cf. Ref [6])
Ma	0.83	Cruise Mach number

As indicated in Fig. 3, the integration of the SG does not rely on other methods, as it solely requires the wing geometry and the current freestream conditions. However, for a sustainable improvement of the database toolchain, the future target is to calibrate its data and derive insights into enhancing the transformation methods used on section level. Most conveniently, this would include comparison and subsequent adaption of section polars at given spanwise positions. Thereby, crossflow influences as well as inaccuracies of transformation rules and the transition prediction could be analyzed and eventually calibrated. In the LowFi-toolchain, wing and section levels are connected via local lift distributions calculated with LILI (see Sec. 2.3). Hence, a prerequisite to compare the data is that the lift distributions of wings with integrated HLFC and VC technologies are within an acceptable error margin when computed with LILI and DLR TAU. To get equivalents to viscous and wave drag polars of the database method, the section polars must be extracted from the HiFi data excluding effects of, primarily, induced drag on the pressure distribution. This, however, is not directly possible without significant modeling measures, as the typical drag breakdown available from the CFD solution consists in surface normal and tangential forces, inherently capturing induced drag components in the surface normal force vector alongside viscous and wave drag components. Therefore, extracting the local induced drag component would require spanwise modeling of the induced drag force, e.g. via a Trefftz-Plane analysis, while viscous and wave drag components typically require viscous and shock volume extractions from the three-dimensional CFD solution, associated with an adequate modeling approach for the corresponding components, e.g. via Oswatitsch's formula [30]. These steps introduce further modeling uncertainty to the SG or ROM, for which the extraction of section polars is discarded in the current context.

Nonetheless, the pressure distributions used for transition prediction within STABTOOL at given spanwise stations are suitable for comparison. Whereas usually, the pressure distributions calculated with MSES are provided by the database, they can be substituted with data extracted from a 3D surface solution; this enables multiple analyses of, e.g., the difference between 2D (and subsequently transformed to 3D) and actual 3D pressure distributions, their influence on the transition prediction, and the overall impact of the differences on wing level. The setup and functionality of the underlying POD ROM are presented in Sec. 3.2. Finally, the implementation in MICADO is briefly explained in Sec. 3.3.

DOI: 10.13009/EUCASS2023-384

3.1 Surrogate Modeling

As introduced in Sec. 3 and displayed in Fig. 3, the focus of the implemented SG lies on parametric prediction of the total drag coefficient C_D of the wing. The SG is thereby built upon Gaussian process regression (GPR), making use of the GPR implementations within scikit-Learn [31]. A comprehensive overview of GPR is given in the standard textbook by Rasmussen and Williams [32]. In the following, important aspects for model design and conditioning will be briefly presented. A more detailed study is presented by two of the authors in Ref. [33].
Gaussian process regression is a supervised machine learning technique, based upon probabilistic principles. Advantages of GPR include good generalization properties with little training data, an inherent uncertainty quantification, and an automatic trade-off between model complexity and model fitting. Therefore, it has been chosen in the context of this study.
The goal of a Gaussian process (GP) in a regression context is inferring function values f_*, in the present case the wing drag coefficient C_D, given a parameter combination $\boldsymbol{p}_*$. The known function values f at the sampling parameter combinations $\boldsymbol{p}$ and f_* are assumed to be drawn from a jointly Gaussian distributed set of functions, for which the sought-for function values f_*, can be drawn from the conditional distribution [32]:

$$(\boldsymbol{f_*}|\boldsymbol{p}_*, \boldsymbol{p}, \boldsymbol{f}) \sim \mathcal{N}(k(\boldsymbol{p}_*, \boldsymbol{p})\, k(\boldsymbol{p}, \boldsymbol{p})^{-1}\boldsymbol{f}, k(\boldsymbol{p}_*, \boldsymbol{p}_*) - k(\boldsymbol{p}_*, \boldsymbol{p})\, k(\boldsymbol{p}, \boldsymbol{p})^{-1}k(\boldsymbol{p}, \boldsymbol{p}_*)). \tag{1}$$

The first term within the distribution $\mathcal{N}$ (Eq. 1), thereby constitutes the mean value of the Gaussian process, whereas the second term characterizes its standard deviation, utilized for uncertainty quantification. The function k represents the corresponding entries of the covariance matrix, where in this paper a squared-exponential kernel is applied:

$$k(\boldsymbol{p}, \boldsymbol{p'}) = \sigma_f^2 \exp\left(-\frac{1}{2}\sum_{i=1}^{d}\frac{(p_i - p_i')^2}{\ell_i^2}\right). \tag{2}$$

The kernel function (Eq. 2) is characterized by the hyper-parameters σ_f^2 and ℓ_i, which represent the marginal variance and the length scales of the GP. In the present case, a total of three input dimensions is considered (C_L, δ_{ADHF} and H), for which the hyper-parameter vector $\boldsymbol{\theta}$ of the GP results in $\boldsymbol{\theta} = [\sigma_f^2, \ell_{C_L}, \ell_{\delta_{ADHF}}, \ell_H]$. Training, in the context of GPR, finally refers to optimization of these hyper-parameters, which based upon the sampling data points is achieved through maximizing the log-marginal-likelihood function of the GP.
The training data set for the GPR-SG is generated in a two-step process; first, a sampling plan built on a Latin hypercube sampling strategy is employed for the base sampling points $\boldsymbol{p} \in \mathcal{P}_{cruise}$, which are subsequently computed using the HiFi-toolchain described in Sec. 2.2. Based upon the prediction parameter array $\boldsymbol{p}_*$, adaptive sampling points $\boldsymbol{p}_{adapt}$ are iteratively added to the training data set. The adaptive sampling points $\boldsymbol{p}_{adapt}$, are chosen at the parameter combinations with the maximum estimated mean square error of the GP (see, e.g., Ref. [34]). Consecutively, the normalized root mean square prediction error of the model ϵ_{RMS}, using the updated training data set is assessed with respect to a full factorial test data set, where the cut-off condition for the adaptive sampling strategy is set to $\epsilon_{RMS} < 5 \cdot 10^{-3}$. This is achieved after a total sample size of 54 sampling points, see left panel of Fig. 4. The resulting error density distribution is shown in the mid panel of Fig. 4, with respect to the final sampling size of 54 samples and an intermediate sample size of $n_{SP} = 20$.

3.2 Model Order Reduction

The second coupling approach presented in Fig. 3 focuses on the parametric prediction of pressure coefficient distributions. Within this paper, this is achieved by the application of a reduced order model (ROM) based on Proper Orthogonal Decomposition (POD) and interpolation of the corresponding POD coefficients in the resulting latent space.
As for the GPR-SG, the POD-ROM is based upon the parametric training data set presented in Sec. 3.1. In the present context, c_p-distributions on the surface of the wing are used to construct the snapshot matrix $W = (\boldsymbol{W}^1, \ldots, \boldsymbol{W}^{n_{sp}}) \in \mathbb{R}^{n_{GP} \times n_{SP}}$, where n_{GP} corresponds to the number of surface nodes contained in the CFD mesh and n_{SP}, as before, to the number of sampling parameter combinations. The low-dimensional embedding of W is subsequently derived via a singular value decomposition (SVD):

$$W = U\Sigma V^T, \tag{3}$$

where the matrices $U \in \mathbb{R}^{n_{GP} \times n_{GP}}$ and $V \in \mathbb{R}^{n_{SP} \times n_{SP}}$ are orthogonal bases of W, and $\Sigma \in \mathbb{R}^{n_{GP} \times n_{SP}}$ contains the corresponding singular values $\sigma_1, \ldots, \sigma_{n_{SP}}$ in the diagonal of the first n_{SP} rows of Σ, for the typical case of $n_{SP} < n_{GP}$.

DOI: 10.13009/EUCASS2023-384

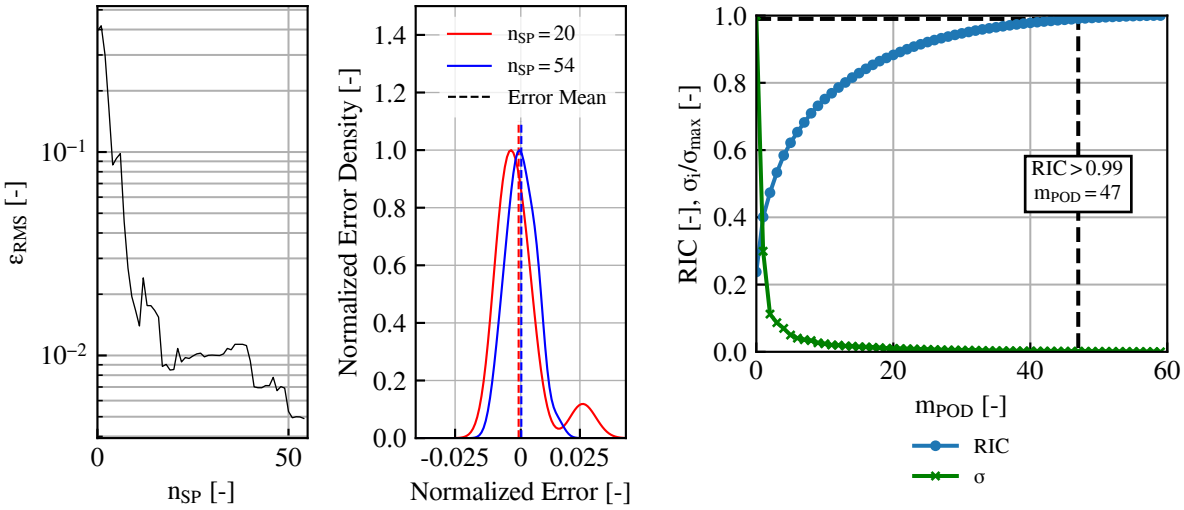

Figure 4: Left panel: Development of the normalized root mean square error ϵ_{RMS} of the predictions of the GPR-SG at the test points with respect to increasing sample size n_{SP}. Mid panel: Error density distribution for model predictions with a sample size of $n_{SP} = 20$ and $n_{SP} = 54$, alongside the corresponding means of the prediction errors. Right panel: Relative information content of POD basis with increasing number of modes m_{POD}, alongside development of the normalized singular values σ_i.

In the context of the POD snapshot method [35], the columns of U reflect the so-called POD modes. Typically, the reduced SVD is computed in the context of the POD, and only the first m_{POD} columns of U are maintained for representation of the data set. The number of maintained POD modes m_{POD} is determined according to the relative information content criterion (RIC) surpassing a threshold of $RIC \geq 0.99$ [36]:

$$RIC = \frac{\Sigma_{i=1}^{m_{POD}} \sigma_i^2}{\Sigma_{j=1}^{n_{SP}} \sigma_j^2}. \tag{4}$$

The RIC criterion builds upon the singular values σ_i in Σ being inherently ordered with decreasing magnitude, thus reflecting the significance of the different POD modes contained in U for rebuilding the snapshot matrix W. An overview of the course of the RIC over the number of POD modes and the corresponding normalized magnitudes of the singular values is given in the right panel of Fig. 4, where the threshold value of $RIC \geq 0.99$ is reached after inclusion of $m_{POD} = 47$ modes into the modal basis.
Finally, the sought-after representation of the snapshot matrix in terms of a linear combination of the POD modes $\boldsymbol{U}^1, \ldots, \boldsymbol{U}^{m_{POD}}$ with POD coefficients $\boldsymbol{a}^1, \ldots, \boldsymbol{a}^{n_{SP}}$ is given as:

$$\boldsymbol{W}^i \approx \sum_{j=1}^{m_{POD}} a_j^i \boldsymbol{U}^j, \tag{5}$$

where in this work the POD coefficients are computed as $a_j^i = \sigma_j V_i^j$.
Since the columns of the snapshot matrix W represent c_p-distributions at the corresponding sample parameter combinations $\boldsymbol{p}^i$, the i-th POD coefficient vector $\boldsymbol{a}^i$ is also a function of $\boldsymbol{p}^i$, namely indicating the scaling of the invariant POD modes in Eq. 5 to reconstruct $\boldsymbol{W}(\boldsymbol{p}^i)$. Therefore, given the surface solutions of the above introduced training set, a surface solution $\boldsymbol{W}^*$ at an unknown parameter combination $\boldsymbol{p}^*$ can be reconstructed via interpolation in the POD coefficient space, by determination of $\boldsymbol{a}^* = \boldsymbol{a}(\boldsymbol{p}^*)$ and subsequent back mapping from the latent space to the original space using Eq. 5. In the sense of model order reduction, the reconstruction problem is therefore shifted to determination of the corresponding POD coefficient vectors $\boldsymbol{a}(\boldsymbol{p}^*)$ [37].
The above-described method was introduced by Bui-Tanh et al. [38] with focus on aerodynamic applications. Due to the linearity of the method, back mapping from latent to original space is straightforward (Eq. 5), while the non-intrusive character of the method makes it very cheap to evaluate and to extend, allowing for efficient integration of the POD-ROM into the LowFi-environment.

DOI: 10.13009/EUCASS2023-384

3.3 Model integration in MICADO

Both presented models are coupled to the aerodynamic module of MICADO via stand-alone executables with their input and output being read from and stored to data files. The input data comprises the parameters specified in Tab. 1, where for the sweep parameters $[C_L, \delta_{ADHF}, H]$ the respective step widths are additionally prescribed. In addition, the ROM requires information about the spanwise stations for which the section analyses are conducted. Querying data from both models does not considerably increase the runtime of the aerodynamic module. Once the output data is read, it is checked whether HiFi data is available for the current set of lift coefficient, Mach number, and flight altitude. If data is available, the model substitutes the LowFi data as illustrated in Fig. 3. Finally, drag coefficients from the remaining aircraft components not considered in the HiFi setup are added; this ultimately leads to the aircraft polar, which can subsequently be used within the MICADO loop.
In the current HiFi setup, only the isolated wing geometry is calculated (see Sec. 2.2). During initial test studies, the results showed a significant influence of the rectangular segment (S1 in Fig. 2). For a more realistic calculation of the aerodynamics of the wing, the following handling is implemented: The SG/ROM models provide data only for the wetted surface, hence, for the segments S2-S4. For a consistent comparison with the LowFi approach, the induced drag of the thereby neglected fuselage segment is extracted from the LILI results. In the common LILI approach, this segment is considered to map the influence of the fuselage onto the load distribution. In future studies, other components, such as the tailplane and fuselage, will be considered in the HiFi setup, making this handling obsolete.

4. Results

The following section presents selected results for the cruise flight envelope defined in Tab. 1. Firstly, isolated results of the models are presented and compared to HiFi results in Sec. 4.1. Section 4.2 deals with the comparison of model results with corresponding LowFi results on overall aircraft level.

4.1 Isolated Model Results

GPR-SG. A predicted response surface of the trained GPR-SG model for varying ADHF deflection angles δ_{ADHF} and wing lift coefficients C_L, at an altitude of $H = 35\,000$ ft is shown in Fig. 5.

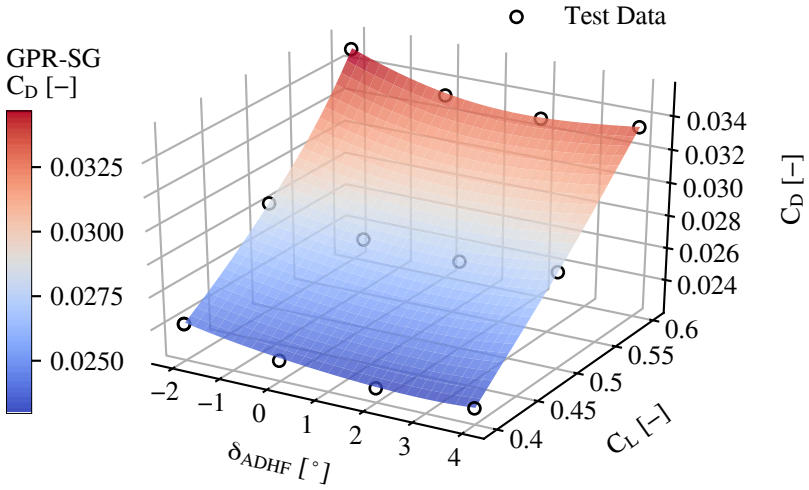

Figure 5: Predicted C_D-response surface by the GPR-SG for varying ADHF deflection angles δ_{ADHF} and lift coefficients C_L at $H = 35\,000$ ft. Additionally, the C_D values of the corresponding test data $\mathcal{P}_{Test}$ set are indicated. Adapted from Ref. [33].

The quantitative agreement of the predicted drag coefficients with the test data set is accordingly reflected in the response surface. The normalized model hyper-parameters result in $\boldsymbol{\theta} = [0.00551^2, 0.459, 0.872, 60.6]$, allowing for direct interpretation of response surface sensitivities with respect to the different parameter dimensions. The length

DOI: 10.13009/EUCASS2023-384

scale parameters ℓ_i thereby express the width of the kernel function (Eq. 2) in the corresponding parameter dimension, where a short length scale indicates rapid changes of the response surface and a long length scale slow changes of the response surface in the associated parameter dimension. Therefore, the model reflects the expected physical effects, namely C_D being most sensitive to changes in C_L, a reduced impact of δ_{ADHF} on C_D, and the altitude H having a relatively small impact on C_D.

POD-ROM. As introduced in Sec. 3.2, the main focus of the POD-ROM lies on parametric prediction of surface pressure coefficient distributions. The POD-ROM thereby uses the same training data set as the GPR-SG, making use of the space-filling properties of the employed Latin Hypercube sampling strategy alongside the uncertainty quantification of the GPR-SG for determination of adaptively added sampling parameter combinations.
Concerning the practical application, the mean value of the c_p-snapshots is initially subtracted from the columns of the snapshot matrix W, after which the corresponding modal bases are computed using the strategy described in Sec. 3.2. An example for a predicted pressure distribution on the suction side of the wing at the test set parameter combination $\boldsymbol{p}^* = [0.5, 0°, 35\,000\ \text{ft}]$ compared to the CFD (surface) solution is presented in Fig. 6.

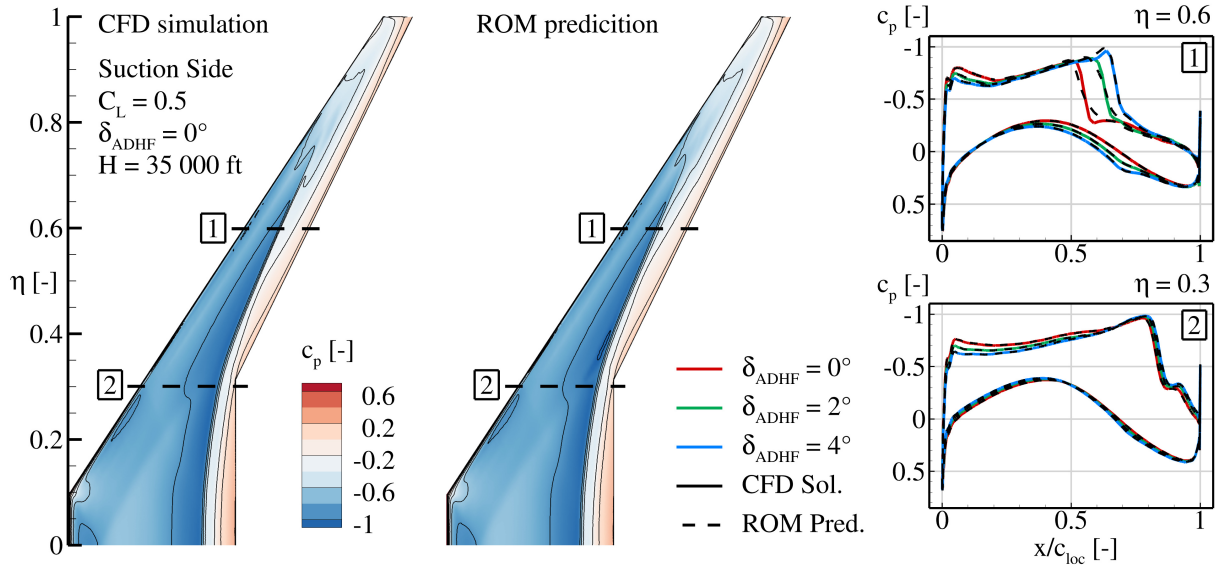

Figure 6: Comparison of pressure coefficient distribution computed via CFD (left panel) with POD-ROM prediction (mid panel) at a parameter combination of $\boldsymbol{p}^* = [0.5, 0°, 35\,000\ \text{ft}] \in \mathcal{P}_{val}$. The right panels additionally show extracted chordwise c_p-distributions at spanwise stations of $\eta = 0.3$ and 0.6, under variation of the ADHF deflection angle δ_{ADHF}.

The predicted pressure coefficient shows high qualitative agreement with the CFD solution. The c_p-distribution is characterized by a strong compression shock limiting the region of streamwise flow acceleration. A lambda shock structure develops on the suction side of the wing, which is correspondingly reflected by the POD-ROM prediction. For the displayed baseline case of $\delta_{ADHF} = 0°$, the shock front generally moves upstream with increasing spanwise positions. Deflecting the ADHF incrementally leads to an alignment of the shock front with the upstream limit of the spoiler, as depicted in the sectional c_p-distributions in the right panels of Fig. 6. The solid lines thereby show the streamwise c_p-distributions for three ADHF deflection angles comprised in the test data set, whereas the corresponding dashed lines represent the distributions extracted from the surface c_p predictions of the POD-ROM. Within the sectional cut at $\eta = 0.3$, no visual distinction between the CFD solutions and the POD-ROM predictions is possible. Considering the spanwise station $\eta = 0.6$, the POD-ROM accordingly predicts the downstream shift in shock location with increasing δ_{ADHF}, where shock positions and strengths agree well between predictions and CFD data. Deviations are observable in the predicted streamwise extent of the shocks, which stem from the underlying assumption of the POD method, that the flow solution lies on a linear subspace spanned by the POD modes. Therefore, the linear superposition of the POD modes according to the interpolated POD coefficients typically shows inaccuracies in reproducing strongly non-linear phenomena, as reflected in the present case for the extent of the shock waves. Nevertheless, regarding the accuracy requirements posed in the context of near real-time integration of the HiFi-data into the LowFi-environment, the predictions show satisfactory results.
As described in Sec. 3, coupling of the POD-ROM into the aerodynamic module of MICADO further requires determining the spanwise lift coefficient distributions $C_l(y)$ for the requested parameter combinations $\boldsymbol{p}^*$. Therefore,

DOI: 10.13009/EUCASS2023-384

the sectional normal force components in x- and z-directions are integrated, readily available from the predicted c_p-distributions and the surface normal vectors of the CFD mesh. Since the sweep parameters within the SG/ROM and the corresponding simulations are set to the lift coefficient of the wing, the corresponding angles of attack α are additionally predicted by the GPR-SG for the requested parameter combination $\boldsymbol{p}^*$[4]. The according force vectors in x- and z-directions are then rotated accordingly into the aerodynamic frame. For completeness, the modal basis is extended to also include the tangential force components in x- and z-directions, accounting for the corresponding viscous lift component. Nevertheless, the x-component of the tangential force vector is of negligible magnitude after rotation into the aerodynamic frame. The corresponding z-component is orders of magnitude smaller than the pressure induced complement, for which there is hardly a contribution to the lift force vector.
Predicted spanwise load and C_l distributions are displayed in Fig. 7 (dashed lines), and compared to the corresponding distributions extracted from the test data set (solid lines) for varying global lift coefficients C_L and ADHF deflection angles δ_{ADHF}. For the set of lift coefficients, the presented baseline case is $\delta_{ADHF} = 0°$, while the deflection angle is increased to $\delta_{ADHF} = 2°$ and $\delta_{ADHF} = 4°$ as indicated by the arrow.

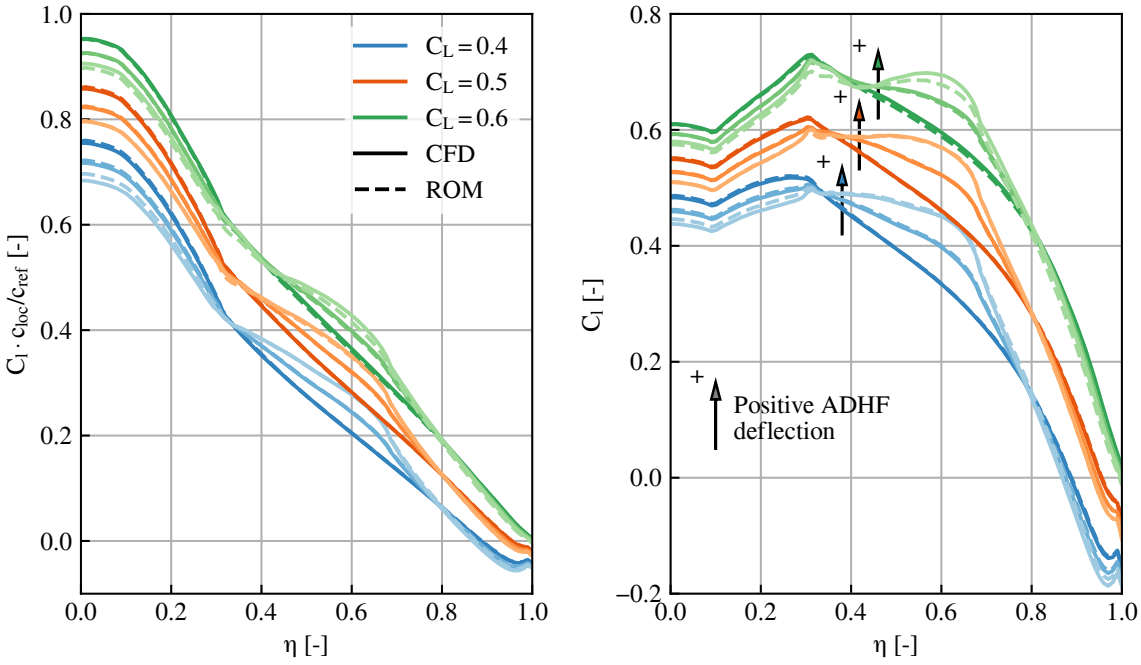

Figure 7: Comparison of aerodynamic loads (left panel) and local C_l distributions (right panel) extracted from CFD solutions (solid line) of the test data set with POD-ROM predictions (dashed line) at $H = 35\,000$ ft. The comparisons are drawn at wing lift coefficients of $C_L = [0.4; 0.5; 0.6]$ for varying ADHF deflection angles of $\delta_{ADHF} = [0°; 2°; 4°]$.

The flow phenomena are reflected throughout all compared cases. A shift in load and corresponding local C_l into the region of the deflected ADHF is observable after force integration. Best agreement between predictions and HiFi-data is observable for $C_L = 0.5$, while deviations arise for cases at the edges of the envelope at $C_L = 0.4$ and $C_L = 0.6$. Especially the combination of $C_L = 0.6$ with the highest flap deflection angle of $\delta_{ADHF} = 4°$ results in more relevant deviations, which can again be attributed to non-linear phenomena playing a major role in cases of high local loads.

4.2 Comparison of the Results

For the database method, an aerodynamic 2D database is set up for all relevant airfoils, including the VC airfoils with deflection angles from Tab. 1. As stated in Sec. 3, similar lift distributions are the prerequisite for consistent method comparison. Although good agreement between LILI and DLR TAU for wings with different VC deflections was demonstrated by the authors in Ref. [39], the meanwhile replaced root airfoil (A1 in Fig. 2) results in non-negligible deviations, illustrated on the left panel in Fig. 8.

[4]Within the DLR TAU Code, the mesh and thus the reference configuration are expressed with respect to a body fixed frame, while the aerodynamic frame is rotated by the angle of attack α to match the prescribed C_L.

DOI: 10.13009/EUCASS2023-384

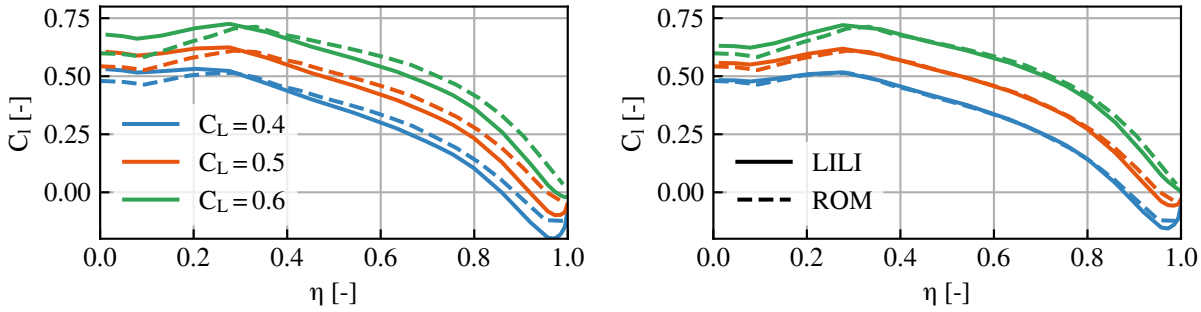

Figure 8: Comparison of local C_l distributions predicted by LILI (solid lines) and extracted from CFD solutions (dashed lines) before (left panel) and after (right panel) adjustment of twist distribution at H = 35 000 ft. The comparisons are drawn at wing lift coefficients of $C_L = [0.4; 0.5; 0.6]$ for $\delta_{ADHF} = 0°$.

The deviation is attributed to viscous effects playing a dominant role in the HiFi solution, namely the shock induced recirculation zone and associated thickening of the boundary layer in inboard stations of the wing leading to viscous decambering effects, which are not captured by the potential flow solver LILI. Therefore, the local lift distribution of $C_L = 0.5$, extracted from CFD data, is initially approximated via geometric twist adjustment utilizing an automatic approach developed at ILR [40]; this results in good agreement over the range of relevant lift coefficients, as shown on the right panel of Fig. 8. Using the adjusted twist distribution for all LowFi calculations ensures a consistent comparison with the HiFi data from both SG and ROM.

GPR-SG and Database Method. Upon integrating the GPR-SG into MICADO, the drag coefficients derived from the LowFi methods for the wetted wing surface are replaced. Subsequently, the neglected induced drag contribution of the fuselage segment and any missing drag from the other components of the aircraft are added (see Sec. 3.3). Figure 9 shows deviations of the overall aircraft polars when computed with the GPR-SG and the database method in MICADO.[5]

The left panel depicts the drag polars of the aircraft, with solid and dashed lines for the database and GPR-SG methods, respectively. In addition, different colors highlight the ADHF deflections. Notably, all polars derived from the database method are shorter in terms of maximum C_L. The discrepancy arises from limitations in the analysis of 2D airfoils, which occur even if the wing performs well in 3D analyses. This phenomenon was already highlighted by the authors in Ref. [39], resulting in reduced $C_{l,max}$ values of the sectional polars retrieved from the database. Furthermore, all polars exhibit substantial shifts towards lower drag coefficients when compared to their counterparts resulting from the GPR-SG integration. The shifts originate from significant deviations in the pressure distributions between LowFi and HiFi, as exemplary shown for two stations ($\eta = 0.313$ and $\eta = 0.68$) of the clean wing and $C_{L,aircraft} = 0.5$ in Fig. 10. It can be observed that the pressure distributions from MSES deviate from those obtained from CFD. While the magnitude of the compression shocks is comparable between the two methods, MSES inaccurately predicts the shock fronts more upstream for both spanwise positions. Consequently, the earlier occurrence of these shocks causes an elevation of the plateau to achieve the same lift. These deviations arise primarily from simplifying three-dimensional flow phenomena and uncertainties stemming from applying transformation rules to geometry and flow characteristics. This weakness of the integrated 2.5D method was already discussed in prior work at ILR and is one reason for initiating the CATeW project (see Sec. 2.3).

Although the polar shifts in Fig. 9 increase with δ_{ADHF}, the relative errors of a single flap setting remain almost constant and range from 7 % to 14 %. This relative error range is visualized on the right panel of Fig. 9. Besides the error range being within an acceptable range for the conceptual design phase, the effects of the flap deflections are mostly correctly mapped, as highlighted by the colors on the left panel. With increasing flap deflection, the drag decreases until stagnation at $\delta_{ADHF} = 2°$. The re-increase in drag, and thus the shift to the right at $\delta_{ADHF} = 4°$ is also correspondingly reflected. Therefore, comparing the database and GPR-SG methods yields two conclusions: On the one side, the LowFi methodology cannot accurately predict absolute values. On the other side, however, sensitivities are correctly captured, even when integrating VC and HLFC technologies. These findings align with the intended scope of 2.5D methods, which focus on determining relative deltas and accurately mapping sensitivities across different use cases,

[5]Note that the incidence angle of the horizontal tailplane is deliberately set to have a negligible effect on the lift in the relevant range of lift coefficients; thus, $C_{L,aircaft} \approx C_{L,wing}$.

DOI: 10.13009/EUCASS2023-384

rather than providing precise absolute values. Nevertheless, integrating higher fidelity models, such as the GPR-SG presented here, into a conceptual aircraft design environment offers an excellent approach to balance sophisticated aerodynamic predictions and runtime efficiency for rapid exploration of design spaces.

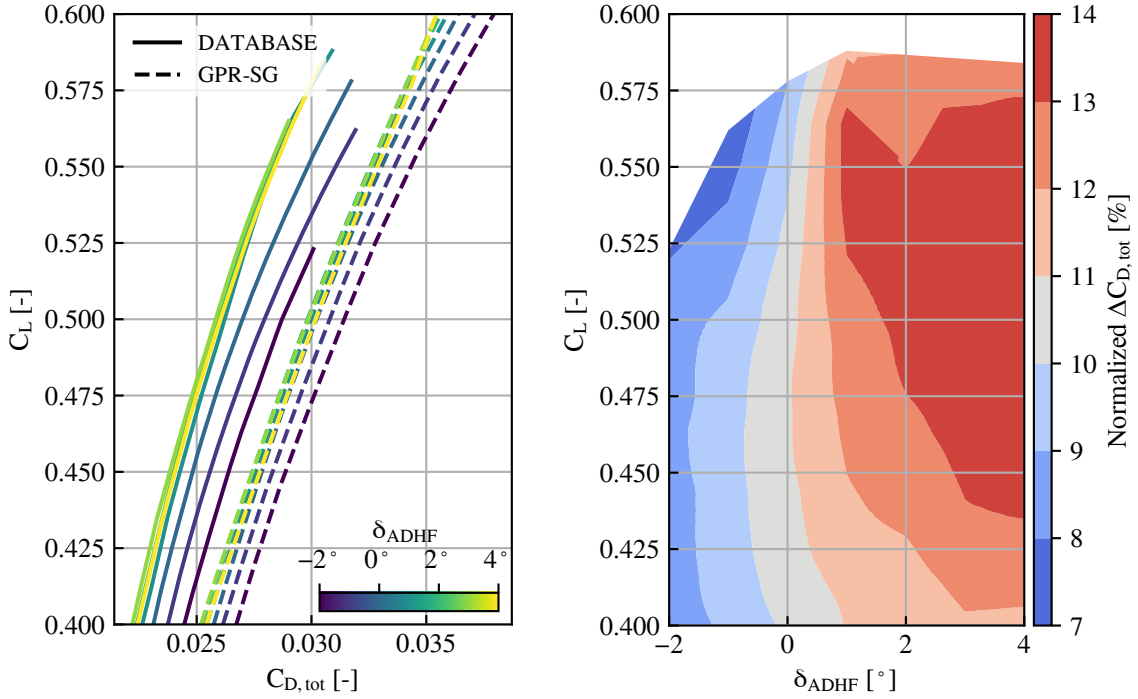

Figure 9: Comparison of aircraft polars predicted using data from the database method (solid lines) and from the GPR-SG (dashed lines) for varying ADHF deflection angles δ_{ADHF} at H = 35 000 ft (left panel). The right panel visualizes the corresponding normalized errors of the drag total drag coefficient $\Delta C_{D,tot}$.

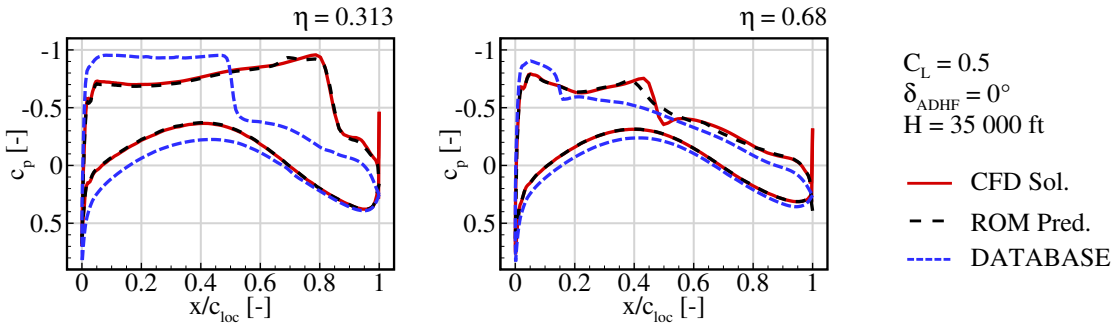

Figure 10: Comparison of chordwise c_p-distributions at spanwise stations of η = 0.313 and 0.68, predicted with CFD/ROM and database method, i.e. 2D flow solver MSES and transformation rules.

ROM and Database Method. This section concludes by showing the possibilities offered by integrating the ROM. Note that how the ROM is integrated solely influences predicting the transition position within STABTOOL (see Fig. 3). The transition position calculated with the pressure distribution from the ROM is fed back to the database to query aerodynamic data. Hence, the inaccuracies in absolute values demonstrated in the previous paragraph remain. However, the purpose of the ROM is to provide sophisticated data, which can, in turn, be used to calibrate the transformation methods. Such studies cannot be conducted with the GPR-SG, as it only provides absolute values. Figure 11 shows the amplification of N_{CF}- and N_{TS}-factors for the sections used in Fig. 10. In addition to the clean wing, results for a deflection angle of $\delta_{ADHF} = 2°$ are shown in the bottom panels.

DOI: 10.13009/EUCASS2023-384

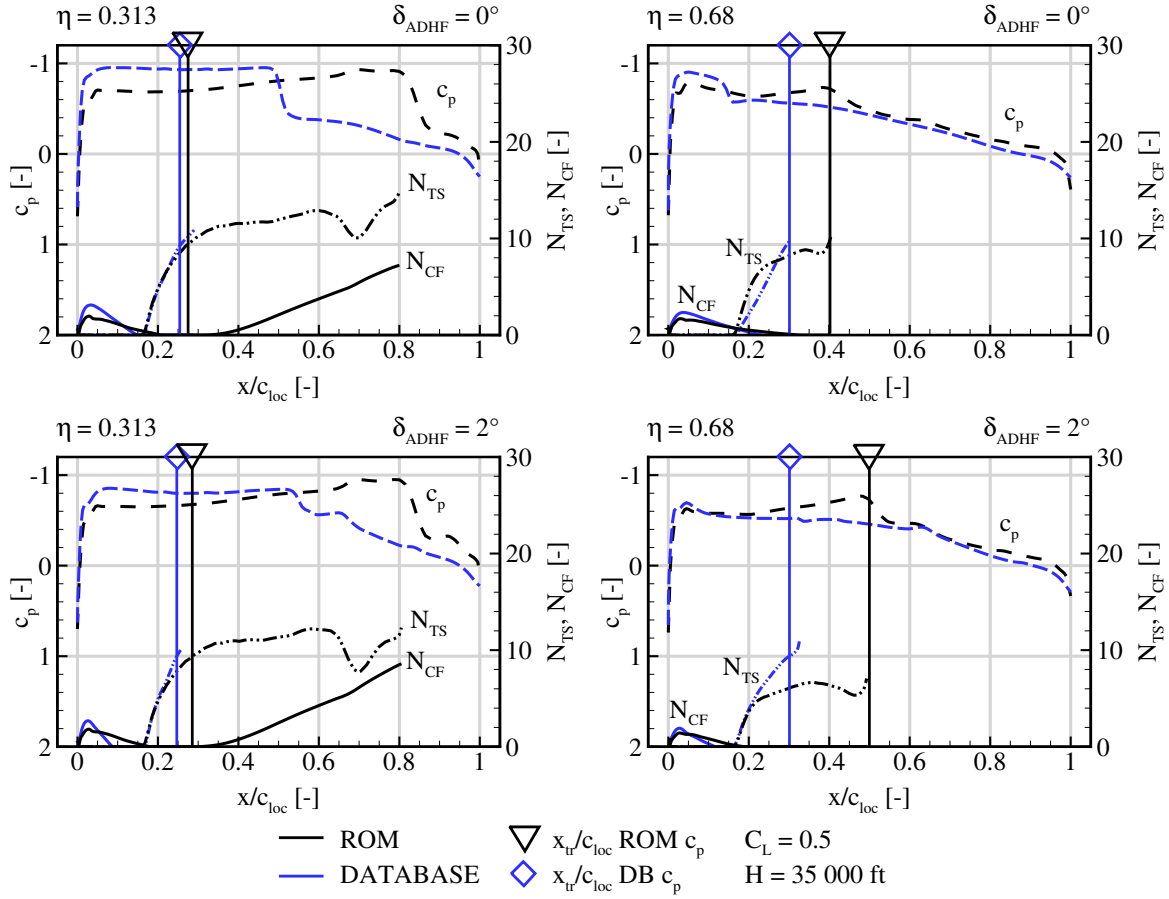

Figure 11: Comparison of N-factor development for spanwise stations of $\eta = 0.313$ (left panel) and $\eta = 0.68$ (right panel) and two flap settings, alongside predicted transition positions.

For the spanwise position $\eta = 0.313$, the deviations in the pressure distribution do not result in considerable changes in the predicted transition positions. Although the suction ahead of the front spar sufficiently damps CFI and TSI, the N_{TS}-factors reach critical values shortly behind the suction area due to unfavorable pressure gradients. Moreover, the flap deflection does not boost the laminar performance at this section. In this case, the lack of synergy effects is mainly due to the limited effect of the deflection on the pressure distribution, as highlighted in Fig. 6. However, the deviations in the pressure distributions at $\eta = 0.68$ result in differences in predicting the transition position in STABTOOL. The gradients of the pressure distributions from the database result in N_{TS}-factors reaching the critical boundary at $x/c_{loc} \approx 0.29$ for both the clean and the deflected airfoil. Contrary to this, the pressure gradients of the clean wing predicted by the ROM result in a shifted transition position at $x_{tr}/c_{loc} \approx 0.4$, again only triggered by TSI. Deflecting the flap by 2° suppresses TSI even further, resulting in a transition through flow separation at the compression shock at $x_{tr}/c_{loc} \approx 0.5$. Hence, not only the absolute drag values but also the predicted transition positions can be improved if the pressure distributions provided by the ROM are used for accurate mapping of three-dimensional flow phenomena. In Ref. [28], successful calibration of the transformation methods was already demonstrated for an HLFC retrofit design using HiFi data; this data, however, was only available for one polar point. The ROM substantially augments the calibration possibilities by encompassing various parameters. Consequently, future studies can strive towards achieving a more comprehensive calibration enhancement.

5. Summary and Conclusions

Within this paper, different approaches for coupling of high-fidelity (HiFi) computational fluid dynamics (CFD) results into the low-fidelity (LowFi) aerodynamic module of the overall aircraft design (OAD) environment MICADO have been presented. The application case is the wing of a reference transonic transport aircraft configuration, which incorporates a technology coupling of hybrid laminar flow control (HLFC) and variable camber (VC) systems, the latter

DOI: 10.13009/EUCASS2023-384

being realized through deflections of an Adaptive Dropped Hinge Flap (ADHF). The analyses are performed within the framework of the research project CATeW (*Coupled Aerodynamic Technologies for Aircraft Wings*), where the potential for aerodynamic drag reduction through the synergistic application of the above mentioned technology coupling is assessed on the respective fidelity levels.

After presenting the HiFi- and LowFi-computational frameworks, different coupling strategies for parametric introduction of driving aerodynamic quantities into the LowFi-toolchain are discussed. Depending on the desired abstraction level, the output parameters of the models consist in prediction of the total wing drag coefficient C_D, or prediction of the surface pressure coefficient distribution c_p on the wing. The input parameters comprise the same quantities for both cases and are derived from the intended cruise flight envelope, consisting in a lift coefficient range of $C_L = [0.4; 0.6]$, the ADHF deflection angles $\delta_{ADHF} = [-2°; 4°]$, flight altitudes of $H = [33\ 000\ \text{ft}; 39\ 000\ \text{ft}]$, and a constant Mach number of $\text{Ma}_{\text{cr}} = 0.83$, alongside a constant suction coefficient of $C_q = -12 \cdot 10^{-4}$.

For prediction of the total wing drag coefficient, a surrogate (SG) model based on Gaussian process regression (GPR) is implemented. The model is trained using a space filling sampling strategy alongside adaptively added samples, and is able to accurately predict the wing drag coefficient throughout the envisaged parameter envelope, when compared to a dedicated test data set.

Prediction of the surface c_p-distribution is achieved via application of the Proper Orthogonal Decomposition (POD) approach for derivation of a reduced order model (ROM), and according parametric interpolation in the POD coefficient space. Again, the model shows good agreement in its predictive capabilities, when being compared to the surface pressure distributions of the test data set. Inaccuracies arise at parameter combinations characterized by strongly nonlinear phenomena (at the edges of the considered envelope); nonetheless, the results are satisfactory for the intended application.

Comparison of the SG/ROM-enhanced and the LowFi-toolchains within MICADO underlined that the LowFi approach, which combines a 2D airfoil database with the 3D transition prediction suite STABTOOL through various transformation rules, can correctly capture sensitivities for different use cases, even with integrated HLFC and VC technologies. However, when compared to the SG-enhanced toolchain, significant offsets in the drag polars of the aircraft were observed. Furthermore, the integration of the ROM emphasized the potential for more precise transition predictions (within the limitations of linear stability theory). The findings demonstrate the improvement in accuracy achieved by incorporating surrogate and reduced order models generated from HiFi data in a conceptual aircraft design environment such as MICADO. Contrary to single-point comparisons with available HiFi data, the presented models allow rapid explorations of design spaces while maintaining aerodynamic prediction accuracy. This advantage ideally suits them for integration into the conceptual aircraft design phase.

6. Acknowledgments

The funding of the herein presented investigations within the LuFo VI-1 project CATeW (Coupled Aerodynamic Technologies for Aircraft Wings, FKZ: 20E1917A/B) by the German Federal Ministry for Economic Affairs and Climate Action (BMWK) is gratefully acknowledged. The authors deeply appreciate the German Aerospace Center (DLR) for providing the DLR TAU Code used for the numerical HiFi-investigations. Moreover, the authors would like to thank the Gauss Centre for Supercomputing e.V. (`www.gauss-centre.eu`) and the Leibniz Supercomputing Center (LRZ, `www.lrz.de`) for providing computing time on the GCS Supercomputer SuperMUC-NG.

References

[1] Zheng, X.S., Rutherford, D.: Fuel Burn of New Commercial Jet Aircraft: 1960 to 2019, White paper (2020)

[2] Risse, K., Anton, E., Lammering, T., Franz, K., Hörnschemeyer, R.: An Integrated Environment for Preliminary Aircraft Design and Optimization. In: American Institute of Aeronautics and Astronautics (ed.) 53rd AIAA/ASME/ASCE/AHS/ASC Structures, Structural Dynamics and Materials Conference: SciTech 2012, vol. AIAA 2012-1675 (2012). `https://doi.org/10.2514/6.2012-1675`

[3] Schültke, F., Aigner, B., Effing, T., Strathoff, P., Stumpf, E.: MICADO: Overview of Recent Developments within the Conceptual Aircraft Design and Optimization Environment. In: Deutsche Gesellschaft für Luft- und Raumfahrt - Lilienthal - Oberth e.V. (ed.) 69. Deutscher Luft- und Raumfahrtkongress (2020). `https://doi.org/10.25967/530093`

[4] Schültke, F., Stumpf, E.: UNICADO - Development and Establishment of a University Conceptual Aircraft Design Environment. In: Deutsche Gesellschaft für Luft- und Raumfahrt - Lilienthal - Oberth e.V. (ed.) 69. Deutscher Luft- und Raumfahrtkongress (2020). `https://doi.org/10.18154/RWTH-2021-09317`

DOI: 10.13009/EUCASS2023-384

[5] Wöhler, S., Hartmann, J., Prenzel, E., Kwik, H.: Preliminary aircraft design for a midrange reference aircraft taking advanced technologies into account as part of the AVACON project for an entry into service in 2028. In: Deutsche Gesellschaft für Luft- und Raumfahrt - Lilienthal - Oberth e.V. (ed.) 67. Deutscher Luft- und Raumfahrtkongress (2018). https://doi.org/10.25967/480224

[6] Jentys, M., Breitsamter, C.: Transitional flow modelling of a hybrid laminar flow control and variable camber transonic transport aircraft wing. In: Proceedings of the 33rd Congress of the International Council of the Aeronautical Sciences, Stockholm, Sweden (2022)

[7] Reckzeh, D.: Multifunctional Wing Moveables: Design of the A350XWB and the Way to Future Concepts. In: Proceedings of the 29th Congress of the International Council of the Aeronautical Sciences, St. Petersburg, Russia (2014)

[8] Strüber, H.: The Aerodynamic Design of the A350 XWB-900 High Lift System. In: International Council of the Aeronautical Sciences (ed.) Proceedings of the 29th Congress of the International Council of the Aeronautical Sciences, St. Petersburg, Russia (2014)

[9] Schlichting, H., Gersten, K.: Boundary-Layer Theory. Springer, Berlin, Heidelberg (2017). https://doi.org/10.1007/978-3-662-52919-5

[10] Schwamborn, D., Gardner, A., von Geyer, H., Krumbein, A., Lüdeke, H., Stürmer, A.: Development of the TAU-Code for aerospace applications. In: 50th NAL International Conference on Aerospace Science and Technology (2008)

[11] Alcaraz Capsada, L., Heinrich, R.: Development of the DLR TAU Code for Modelling of Control Surfaces. In: Deutsche Gesellschaft für Luft- und Raumfahrt - Lilienthal - Oberth e.V. (ed.) 67. Deutscher Luft- und Raumfahrtkongress (2018). https://doi.org/10.25967/480018

[12] Grabe, C., Shengyang, N., Krumbein, A.: Transport Modeling for the Prediction of Crossflow Transition. AIAA Journal **56**(8), 3167–3178 (2018). https://doi.org/10.2514/1.J056200

[13] Horstmann, K.-H.: Ein Mehrfach-Traglinienverfahren und seine Verwendung für Entwurf und Nachrechnung nichtplanarer Flügelanordnungen. Ph.D. thesis, Technische Universität Braunschweig (1988)

[14] Horstmann, K.-H., Engelbrecht, T., Liersch, C.: LIFTING_LINE: Version 3.0 Revision: User Manual (2019)

[15] Liersch, C.M., Wunderlich, T.: A fast aerodynamic tool for preliminary aircraft design. In: 12th AIAA/ISSMO Multidisciplinary Analysis and Optimization Conference. American Institute of Aeronautics and Astronautics, Reston, Virigina (2008)

[16] Risse, K.: Preliminary Overall Aircraft Design with Hybrid Laminar Flow Control: Vorentwurf von Flugzeugen mit hybrider laminarer Strömungskontrolle. Ph.D. thesis, RWTH Aachen University (2016)

[17] Raymer, D.P.: Aircraft Design: A Conceptual Approach, 6. edn. AIAA education series. American Institute of Aeronautics and Astronautics, Washington, DC (2018). https://doi.org/10.2514/4.104909

[18] Boppe, C.W.: Aircraft Drag Analysis Methods. In: North Atlantic Treaty Organization (ed.) Special Course on Engineering Methods in Aerodynamic Analysis and Design of Aircraft vol. AGARD-R-783, pp. 7–1750 (1992)

[19] Mason, W.H.: Analytic models for technology integration in aircraft design. In: American Institute of Aeronautics and Astronautics (ed.) Aircraft Design and Operations Meetings (1990)

[20] Drela, M.: A User's Guide to MSES 3.05: User Manual. Massachusetts Institute of Technology (MIT), Cambridge (2007)

[21] Schrauf, G.: COCO: A Program to Compute Velocity and Temperature Profiles for Local and Nonlocal Stability Analysis of Compressible, Conical Boundary Layers with Suction: Technical Report ZARM, Bremen (1998)

[22] Schrauf, G.: LILO 2.1: User's Guide and Tutorial: GSSC Technical Report 6 (2006)

[23] Arnal, D., Casalis, G., Houdeville, R.: Practical Transition Prediction Methods: Subsonic and Transonic Flows. In: Advances in Laminar-Turbulent Transition Modelling: Lecture Series vol. RTO-EN-AVT-151. Rhode St. Genèse, Belgium, pp. 7–1734 (2008)

DOI: 10.13009/EUCASS2023-384

[24] Schrauf, G.: Transition Criteria for HLFC Studies. Technical Report PR1517186, Airbus, Bremen, Germany (2015)

[25] Arnal, D., Juillen, J.C., Reneaux, J., Gasparian, G.: Effect of Wall Suction on Leading Edge Contamination. Aerospace Science and Technology **1**(8), 505–517 (1997). https://doi.org/10.1016/S1270-9638(97)90000-6

[26] Schültke, F., Stumpf, E.: Implementation of an Airfoil Information Database for Usage in Conceptual Aircraft Wing Design Process. In: American Institute of Aeronautics and Astronautics (ed.) AIAA Scitech 2019 Forum, vol. 2019-0814. Reston, Virginia, p. 624 (2019). https://doi.org/10.2514/6.2019-0814

[27] Schültke, F., Stumpf, E.: Cross-flow effects regarding laminar flow control within conceptual aircraft design. Aircraft Engineering and Aerospace Technology: An International Journal (AEAT) **89**(4), 620–631 (2017). https://doi.org/10.1108/AEAT-11-2016-0210

[28] Effing, T., Schültke, F., Stumpf, E.: HLFC-optimized retrofit aircraft design of a medium-range reference configuration within the AVACON project. CEAS Aeronautical Journal **12**(2), 441–456 (2021). https://doi.org/10.1007/s13272-021-00510-0

[29] Effing, T., Schmitz, V., Schültke, F., Peter, F., Stumpf, E.: Combined Application of Hybrid Laminar Flow Control and Variable Camber in Preliminary Aircraft Design. In: Proceedings of the 33rd Congress of the International Council of the Aeronautical Sciences, Stockholm, Sweden (2022). https://doi.org/10.18154/RWTH-2022-11091

[30] Ostieri, M.: Aerodynamic lift and drag breakdown in steady and unsteady flows. Ph.D. thesis, Università degli Studi di Napoli "Federico II" (2017)

[31] Pedregosa, F., Varoquaux, G., Gramfort, A., Michel, V., Thirion, B., Grisel, O., Blondel, M., Prettenhofer, P., Weiss, R., Dubourg, V., Vanderplas, J., Passos, A., Cournapeau, D., Brucher, M., Perrot, M., Duchesnay, E.: Scikit-learn: Machine learning in Python. Journal of Machine Learning Research **12**, 2825–2830 (2011)

[32] Rasmussen, C.E., Williams, C.K.I.: Gaussian Processes for Machine Learning. The MIT Press, Cambridge, MA (2006)

[33] Jentys, M., Breitsamter, C. (in press): Surrogate modeling of hybrid laminar wing aerodynamic coefficients. In: Dillmann, A., Heller, G., Krämer, E., Wagner, C. (eds.) New Results in Numerical and Experimental Fluid Mechanics XIV. Springer, Cham

[34] Forrester, A.I.J., Sóbester, A., Keane, A.J.: Engineering Design Via Surrogate Modelling: A Practical Guide. John Wiley & Sons, Ltd. (2008)

[35] Sirovich, L.: Turbulence and the dynamics of coherent structures. I - Coherent structures. II - Symmetries and transformations. III - Dynamics and scaling. Quarterly of Applied Mathematics - QUART APPL MATH **45** (1987). https://doi.org/10.1090/qam/910462

[36] Winter, M.: Nonlinear aerodynamic reduced-order modeling using neuro-fuzzy approaches. Ph.D. thesis, Technical University of Munich (2021). https://doi.org/10.13140/RG.2.2.29909.09440

[37] Franz, T.: Reduced-order modeling for steady transonic flows via manifold learning. Technical report, Technische Universität Braunschweig (2016). https://elib.dlr.de/104061/

[38] Bui-Thanh, T., Damodaran, M., Willcox, K.: Proper Orthogonal Decomposition Extensions for Parametric Applications in Compressible Aerodynamics, (2003). https://doi.org/10.2514/6.2003-4213

[39] Jentys, M., Effing, T., Breitsamter, C., Stumpf, E.: Numerical analyses of a reference wing for combination of hybrid laminar flow control and variable camber. CEAS Aeronautical Journal **13**(4), 989–1002 (2022). https://doi.org/10.1007/s13272-022-00598-y

[40] Effing, T., Peter, F., Stumpf, E., Hornung, M.: Approach for the Aerodynamic Optimization of the Twist Distribution of Arbitrary Wing Geometries on Conceptual Aircraft Design Level. In: Deutsche Gesellschaft für Luft- und Raumfahrt - Lilienthal - Oberth e.V. (ed.) 70. Deutscher Luft- und Raumfahrtkongress (2021). https://doi.org/10.25967/550197